J|A|C|S ARTICLES

Published on Web 11/17/2010

Advanced Electron Paramagnetic Resonance and Density Functional Theory Study of a {2Fe3S} Cluster Mimicking the Active Site of [FeFe] Hydrogenase

Alexey Silakov,* Jennifer L. Shaw, Eduard J. Reijerse, and Wolfgang Lubitz*

Max-Planck-Institut für Bioanorganische Chemie, Stiftstrasse 34-36, Mülheim an der Ruhr, 45470, Germany

Received August 30, 2010; E-mail: silakov@mpi-muelheim.mpg.de; lubitz@mpi-muelheim.mpg.de

Abstract: Despite extensive investigations of the active site of the [FeFe] hydrogenases, many details concerning the properties of the "hydrogen converting cluster" are not yet fully understood. The complexity of the so-called H-cluster is one of the main difficulties in studying the properties of its components. The present study is aimed at the mixed-valence EPR active $[Fe_2(\mu\text{-CO})(CO)_3(CN)_2\{MeSCH_2C(Me)(CH_2S)_2\}]^{1-}$ that is structurally closely related to the redox active binuclear part of the H-cluster in its CO-inhibited oxidized state. In this work, we present a characterization of this compound by advanced pulse EPR methods. The accurate determination of the ^{57}Fe, ^{1}H, ^{2}H, ^{14}N, and ^{15}N electron nuclear hyperfine interactions provided a very detailed picture of the electronic structure of this complex. A theoretical study using density functional theory (DFT) calculations identified possible isomers of the compound and further refined the knowledge about its properties. It was found that upon one electron oxidation of the parent Fe(I)−Fe(I) complex, the dominant mixed-valence Fe(I)−Fe(II) species is the one in which the CN ligand of the iron center that is distal to the thioether moves from the basal to the apical position. The unpaired spin distribution of the model complex is found to be clearly different from that of the native H-cluster. These differences are discussed and provide new insight into the functional features of the [FeFe] hydrogenase active site.

Introduction

[FeFe] hydrogenase belongs to a class of enzymes that catalyze the heterolytic splitting of molecular hydrogen and its formation (from protons and electrons).[1] The catalytic site of these enzymes is well conserved between various organisms and has a rather unusual structure consisting of two subclusters: a ferredoxin-like [4Fe4S] cluster and a [2Fe] subcluster linked by a S−Cys ligand (see Figure 1A).[2,3]

Both iron centers in the binuclear subcluster are coordinated by CN^- and CO ligands, stabilizing the metals in a low oxidation state.[4−6] Recently, an EPR spectroscopic study of the H-cluster provided strong evidence for an amine function in the bridging dithiol ligand.[7] On the basis of various spectroscopic and crystallographic studies, it was shown that the distal iron atom has an open coordination site at which the substrate binds to the H-cluster.[2−6,8,9] X-ray crystallographic data also show a hydrophobic channel leading from the surface to this open coordination site for both studied species of [FeFe] hydrogenase from *D. desulfuricans* and *C. pasteurianum*.[2,3]

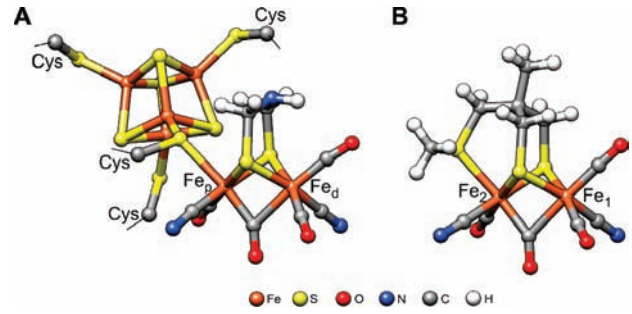

Figure 1. Schematic 3D representation of the H-cluster in the CO-inhibited H_{ox}−CO state (A) and the {2Fe3S} model in one of its isomers (B).

During activation and the catalytic cycle, the H-cluster passes through various states (see Scheme S1 in the Supporting Information). In most of these states, the $[4Fe4S]_H$ subcluster remains formally oxidized (2+). The iron centers in the binuclear subcluster are believed to shuttle between 2+ and 1+.[1,10−12] Several EPR active states ($S = 1/2$) of the active oxidized H-cluster have been detected and attributed to a mixed-valence [Fe(I)−Fe(II)] state of the binuclear subcluster. The so-

(1) Lubitz, W.; Reijerse, E.; van Gastel, M. *Chem. Rev.* **2007**, *107*, 4331–4365.
(2) Nicolet, Y.; de Lacey, A. L.; Vernede, X.; Fernandez, V. M.; Hatchikian, E. C.; Fontecilla-Camps, J. C. *J. Am. Chem. Soc.* **2001**, *123*, 1596–1601.
(3) Peters, J. W.; Lanzilotta, W. N.; Lemon, B. J.; Seefeldt, L. C. *Science* **1998**, *282*, 1853–1858.
(4) Albracht, S. P. J.; Roseboom, W.; Hatchikian, E. C. *J. Biol. Inorg. Chem.* **2006**, *11*, 88–101.
(5) Roseboom, W.; de Lacey, A. L.; Fernandez, V. M.; Hatchikian, E. C.; Albracht, S. P. J. *J. Biol. Inorg. Chem.* **2006**, *11*, 102–118.
(6) Silakov, A.; Kamp, C.; Reijerse, E.; Happe, T.; Lubitz, W. *Biochemistry* **2009**, *48*, 7780–7786.
(7) Silakov, A.; Wenk, B.; Reijerse, E.; Lubitz, W. *Phys. Chem. Chem. Phys.* **2009**, *11*, 6592–6599.
(8) Pandey, A. S.; Harris, T. V.; Giles, L. J.; Peters, J. W.; Szilagyi, R. K. *J. Am. Chem. Soc.* **2008**, *130*, 4533–4540.
(9) Fontecilla-Camps, J. C.; Volbeda, A.; Cavazza, C.; Nicolet, Y. *Chem. Rev.* **2007**, *107*, 4273–4303.

10.1021/ja107793e

called H_{ox} state is characterized by the presence of a bridging CO ligand and is one of the stable intermediates taking part in the catalytic cycle.[1] There is an uncertainty about the coordination of the open coordination site in this state. X-ray data for *D. desulfuricans* suggest that the site is vacant,[13] whereas for the H-cluster in *C. pasteurianum* hydrogenase a water molecule in proximity to the distal iron was suggested.[3,8] However, the fact that the EPR spectra of H_{ox} from both species are almost identical[4,14] indicates a very similar ligand structure.

Free carbon monoxide in solution inhibits the H-cluster in this oxidized state. This results in an EPR active species, $H_{ox}-CO$, in which the open coordination site is occupied by CO[4,5,15] (see Figure 1A). The electronic structure of both H_{ox} and $H_{ox}-CO$ states is characterized by a strong exchange interaction between the $[4Fe4S]_H$ and $[2Fe]_H$ subclusters.[16,17] We have suggested that, although only the binuclear subcluster is directly involved in the chemistry, the presence of the cubane subcluster is also required for catalytic activity.[17]

Interestingly, it was shown that the binuclear subcluster is not bound covalently to the protein apart from the S−Cys link to the $[4Fe4S]_H$ subcluster. It appears as a bioinorganic complex, inserted as a whole into the protein. Recent studies of the maturation processes of [FeFe] hydrogenase indeed indicate that the binuclear subcluster is most probably preformed and then inserted into the apoprotein.[18−20] Consequently, the structure of the binuclear subcluster has inspired many chemists to construct a hydrogen splitting catalyst mimicking the H-cluster. To date, there are many variations of such models, which are described in several excellent reviews.[21−23]

The precursor for most of such model compounds is based on a $(\mu\text{-}SR)_2Fe_2(CO)_6$ construct. It turned out that the nature of the moiety in the dithiol bridgehead considerably influences the catalytic activity of the compound. It has been shown that more electron-withdrawing dithiolate ligands decrease the overpotential of the 2Fe catalysts.[24] Moreover, the catalytic properties can also be considerably improved by creating mixed CO/CN^- or CO/PMe_3 ligation, which, in fact, brings the corresponding model compounds closer to the structure of the H-cluster. Some types of the 2Fe2S compounds were shown to exhibit electrocatalytic proton reduction with substantially reduced overpotential.[21,25,26]

Scheme 1

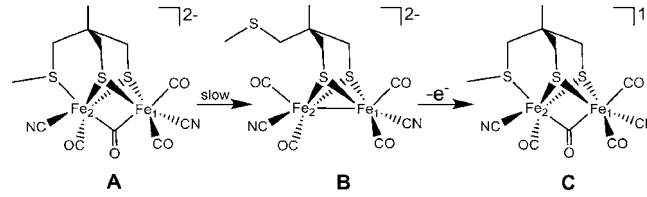

A somewhat different model has been synthesized by Pickett et al.[27,28] Its structure has a remarkable similarity to the binuclear subcluster of the H-cluster in the $H_{ox}-CO$ state (see Figure 1) due to an additional thioether ligand coordinating one of the iron centers and mixed CO/CN ligands coordinating both iron atoms along with a bridging CO moiety. The substitution of two CO ligands of the precursor $[Fe_2(CO)_5\{MeSCH_2C(Me)(CH_2S)_2\}]$ with CN^- ligands proceeds in sequential steps that have been thoroughly investigated by Zampella et al.[29] using DFT methods. It was shown that the resulting compound, $[Fe_2(CN)_2(CO)_3(\mu\text{-}CO)\{MeSCH_2C(Me)(CH_2S)_2\}]^{2-}$ (**A**, see Scheme 1), is stable in the short term and at low temperatures; however, in the long term and at room temperature it transforms into $[Fe_2(CN)_2(CO)_4\{MeSCH_2C(Me)(CH_2S)_2\}]^{2-}$ (**B**). With a large excess of CN, the latter compound can also be obtained directly after the first cyanation step.

Both **A** and **B** compounds are dianions (Fe(I)−Fe(I)) and are EPR silent due to the antiferromagnetic coupling of presumably $S = 1/2$ spins at both irons resulting in a singlet ground state. A one electron oxidation of the Fe(I)−Fe(I) compound (**A** and **B**) leads to a restoration of the thioether coordination to Fe_2 and reformation of the bridging CO ligand (**C**). The resulting monoanion complex **C** was characterized as an EPR active ($S = 1/2$) mixed-valence species with an Fe(I)−Fe(II) oxidation state.

Compound **C** was found to be sufficiently stable to allow spectroscopic examination in a frozen state. EPR measurements of **C** at cryogenic temperatures have indeed shown an EPR signal, indicating a mixed-valence state of the di-iron compound.[27]

More recently, a similar compound with an azadithiolate bridge has been synthesized.[24] In this compound, the tripodal dithiolate thioether is in the form of $\{S_2N\}-(CH_2)_2-S-CH_3$; the thioether was also found to be a pendant ligand in the reduced state and coordinated in the oxidized state. Apparently, the thioether coordinating to one of the iron atoms compensates for the electron loss after oxidation and therefore stabilizes the complex.[24]

Stable mixed-valence Fe(I)−Fe(II) complexes have been also obtained without pendant thioether by introducing another strong σ-donating ligand such as N-heterocyclic carbenes IMes[23,30] or bidentate phosphine ligands[31] at the iron core.

(10) Cao, Z.; Hall, M. B. *J. Am. Chem. Soc.* **2001**, *123*, 3734–3742.
(11) Siegbahn, P. E.; Tye, J. W.; Hall, M. B. *Chem. Rev.* **2007**, *107*, 4414–4435.
(12) Bruschi, M.; Greco, C.; Fantucci, P.; De Gioia, L. *Inorg. Chem.* **2008**, *47*, 6056–6071.
(13) Nicolet, Y.; Piras, C.; Legrand, P.; Hatchikian, C. E.; Fontecilla-Camps, J. C. *Struct. Fold. Des.* **1999**, *7*, 13–23.
(14) Telser, J.; Benecky, M. J.; Adams, M. W. W.; Mortenson, L. E.; Hoffman, B. M. *J. Biol. Chem.* **1986**, *261*, 3536–3541.
(15) Lemon, B. J.; Peters, J. W. *Biochemistry* **1999**, *38*, 12969–12973.
(16) Popescu, C. V.; Munck, E. *J. Am. Chem. Soc.* **1999**, *121*, 7877–7884.
(17) Silakov, A.; Reijerse, E. J.; Albracht, S. P. J.; Hatchikian, E. C.; Lubitz, W. *J. Am. Chem. Soc.* **2007**, *129*, 11447–11458.
(18) Czech, I.; Silakov, A.; Lubitz, W.; Happe, T. *FEBS Lett.* **2010**, *584*, 638–642.
(19) Mulder, D. W.; Boyd, E. S.; Sarma, R.; Lange, R. K.; Endrizzi, J. A.; Broderick, J. B.; Peters, J. W. *Nature* **2010**, *465*, 248–U143.
(20) Mulder, D. W.; Ortillo, D. O.; Gardenghi, D. J.; Naumov, A. V.; Ruebush, S. S.; Szilagyi, R. K.; Huynh, B.; Broderick, J. B.; Peters, J. W. *Biochemistry* **2009**, *48*, 6240–6248.
(21) Tard, C.; Pickett, C. J. *Chem. Rev.* **2009**, *109*, 2245–2274.
(22) Sun, L. C.; Akermark, B.; Ott, S. *Coord. Chem. Rev.* **2005**, *249*, 1653–1663.
(23) Thomas, C. M.; Liu, T. B.; Hall, M. B.; Darensbourg, M. Y. *Inorg. Chem.* **2008**, *47*, 7009–7024.
(24) Schwartz, L. Synthetic [FeFe] Hydrogenase Active Site Model Complexes. Ph.D. Thesis, Uppsala Universitet, Sweden, 2009.
(25) Eilers, G.; Schwartz, L.; Stein, M.; Zampella, G.; De Gioia, L.; Ott, S.; Lomoth, R. *Chem.-Eur. J.* **2007**, *13*, 7075–7084.
(26) Felton, G. A. N.; Vannucci, A. K.; Chen, J. Z.; Lockett, L. T.; Okumura, N.; Petro, B. J.; Zakai, U. I.; Evans, D. H.; Glass, R. S.; Lichtenberger, D. L. *J. Am. Chem. Soc.* **2007**, *129*, 12521–12530.
(27) Razavet, M.; Borg, S. J.; George, S. J.; Best, S. P.; Fairhurst, S. A.; Pickett, C. J. *Chem. Commun.* **2002**, 700–701.
(28) Razavet, M.; Davies, S. C.; Hughes, D. L.; Pickett, C. J. *Chem. Commun.* **2001**, 847–848.
(29) Zampella, G.; Bruschi, M.; Fantucci, P.; Razavet, M.; Pickett, C. J.; De Gioia, L. *Chem.-Eur. J.* **2005**, *11*, 509–520.
(30) IMes = 1,3-bis(2,4,6-trimethylphenyl)imidazol-2-ylidene.
(31) Justice, A. K.; De Gioia, L.; Nilges, M. J.; Rauchfuss, T. B.; Wilson, S. R.; Zampella, G. *Inorg. Chem.* **2008**, *47*, 7405–7414.

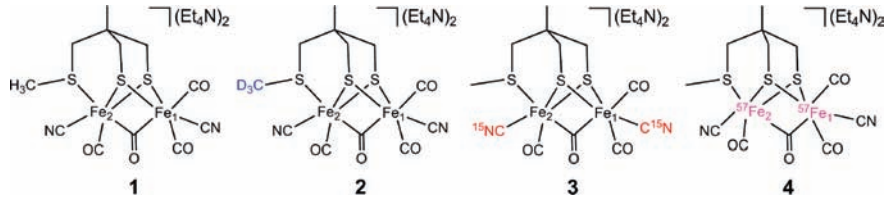

Figure 2. The structures of complexes **1**−**4** indicating isotopic labeling.

Scheme 2. Overview of the Reaction Pathway Used To Prepare Complex **1**

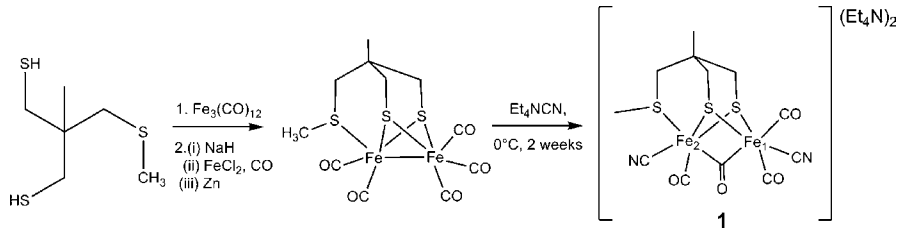

As **C** structurally resembles the binuclear part of the H-cluster, it provides the possibility to take a closer look at the properties of this binuclear construct especially with respect to its electronic structure. We will show that **C** indeed is in an EPR active form, which can be obtained with high purity. The application of advanced EPR methods such as HYSCORE and ENDOR has allowed us to obtain very precise information about the unpaired spin distribution of the model. DFT calculated hyperfine and quadrupole coupling constants were obtained from different levels of theory and compare well with experimental data. The newly obtained data have allowed us to describe the electronic structure of the model in detail and compare its properties with that of the H-cluster in the H_{ox}−CO state. Implications of this study to understanding of the catalytic cycle of the H-cluster are discussed later in this Article.

Materials and Methods

Sample Preparations. Several variants of **A** were prepared with isotopic labels as indicated in Figure 2. These complexes (**1**−**4**) were then oxidized with ferrocinium tetrafluoroborate salt ($FcBF_4$) in butyronitrile or acetonitrile to give the paramagnetic complexes (**1***−**4***), which were frozen to liquid nitrogen temperatures in EPR tubes within 20 s after oxidation.

The unlabeled tripodal dithiolate thioether ligand (H_2L) was prepared as described by Razavet et al.[28,32] Likewise, complexes with a $-CD_3$ pendent arm and those with ^{15}N labeled cyanides were prepared by adaptations of the methods described by Pickett's group.[32]

For compounds **1**−**3**, the precursor $(CO)_5Fe_2L$ was prepared using pathway 1 (see Scheme 2):

$$H_2L + Fe_3(CO)_{12} \rightarrow (CO)_5Fe_2L$$

$Fe_3(CO)_{12}$ (1.05 g, 2.08 mmol) was dissolved in freshly distilled toluene (40 mL) under an inert atmosphere. To this was added a solution of H_2L (370 mg, 2.03 mmol) in toluene (20 mL), and the mixture was stirred at 80 °C for 90 min. The solution was allowed to cool before it was filtered through silica gel, which was washed with further toluene (50 mL). The toluene was removed under vacuum and replaced by acetonitrile (MeCN, 20 mL), and the MeCN was removed, in turn leaving $(CO)_5Fe_2L$ as a red-brown crystalline powder (0.67 g, 63%). The formation of the precursor complexes **1**−**3** was confirmed by IR spectroscopy. Peaks found in these spectra were consistent with the spectra described by Razavet et al.[28]

For ^{15}N labeling of the CN ligands (compound **3**), the following reaction in water was used:

$$KC^{15}N + Et_4NCl \rightarrow Et_4NC^{15}N + KC1$$

$KC^{15}N$ (0.324 g, 4.91 mmol) and Et_4NCl (0.823 g, 4.97 mmol) were dissolved in water (50 mL) and refluxed for one hour. The water was removed under vacuum and replaced with MeCN (50 mL). The mixture was dried over $MgSO_4$ and filtered (KCl was also removed at this stage). The solvent was removed to yield $Et_4NC^{15}N$ as a colorless crystalline solid (0.608 g, 79%). Because of its hygroscopic nature, it was stored in a dry anaerobic glovebox.

An adaptation of a method described by Rauchfuss et al.[33] was used to prepare the ^{57}Fe labeled complex **4** (pathway 2 in Scheme 2). Pathway 1 could not be used to make the ^{57}Fe labeled compound due to the expense and complexity of preparing $^{57}Fe_3(CO)_{12}$. In addition, that method uses an excess of Fe material, which is clearly not cost-effective when isotopic labels are used. The adaptation of the method of Rauchfuss and co-workers uses $^{57}FeCl_2$ (approximately 30% enrichment), which is far more straightforward to prepare, and is used stoichiometrically in the reaction:

$$H_2L + NaH + {}^{57}FeCl_2 + CO + Zn \rightarrow (CO)_5{}^{57}Fe_2L$$

A THF (10 mL) solution of NaH (56 mg, 2.33 mmol) was added to a stirring THF (10 mL) solution of H_2L (213 mg, 1.27 mmol). The reaction was stirred at room temperature for 1 h. To this solution was added a CO saturated solution of $^{57}FeCl_2$ (297.6 mg, 2.33 mmol) in freshly distilled acetone (50 mL). This mixture was allowed to stir at room temperature for 1 h before the addition of Zn dust (158 mg, mol). This mixture was stirred overnight before filtration. The solvent was removed and replaced with CH_2Cl_2 (30 mL). This solution was filtered through silica gel before the solvent was removed to leave $(CO)_5{}^{57}Fe_2L$ as a red-brown solid (565 mg, 46%). The following reactions were identical to pathway 1.

EPR Measurements. Hyperfine sublevel correlation spectroscopy (HYSCORE) experiments[34] were performed using the following MW pulse sequence: $[\pi/2]-\tau-[\pi/2]-t_1-[\pi]-t_2-[\pi/2]-\tau-[\text{echo}]$. For the X-band measurements, the length of the MW pulses $[\pi/2]$ and $[\pi]$ was optimized to the maximum available

(32) Razavet, M.; Davies, S. C.; Hughes, D. L.; Barclay, J. E.; Evans, D. J.; Fairhurst, S. A.; Liu, X. M.; Pickett, C. J. *Dalton Trans.* **2003**, 586–595.

(33) Volkers, P. I.; Boyke, C. A.; Chen, J.; Rauchfuss, T. B.; Whaley, C.; Wilson, S. R.; Yao, H. *Inorg. Chem.* **2008**, *47*, 7002–7008.

(34) Hofer, P.; Grupp, A.; Nebenfuhr, H.; Mehring, M. *Chem. Phys. Lett.* **1986**, *132*, 279–282.

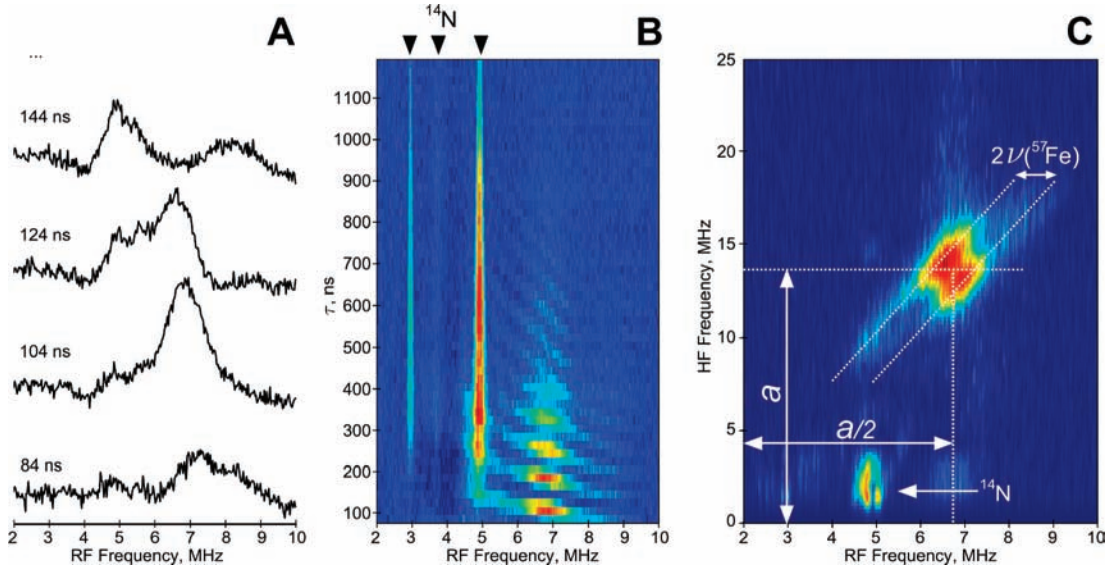

Figure 3. Various steps in the preparation of 2D Mims ENDOR spectra. Individual spectra (A) are collected to form a 2D data array (B); consecutively, the τ-dimension was transformed to the frequency domain by fast Fourier transformation (C) after a baseline correction (see text).

power. The delay τ was varied to maximize the desired parts of the spectra. The starting t_1 and t_2 delays in all measurements were 100 ns. In all cases, a standard four-step phase cycling was used to eliminate unwanted echoes.[35,36]

In the electron nuclear double resonance (ENDOR) experiments, two different pulse sequences were used, the Mims ($[\pi/2]-\tau-[\pi/2]-[\mathrm{RF}]-[\pi/2]-\tau-[\mathrm{echo}]$)[37] and the Davies sequences ($[\pi]_{\mathrm{inv}}-[\mathrm{RF}]-[\pi/2]-\tau-[\pi]-\tau-[\mathrm{echo}]$).[38]

The length of the inversion pulse in the Davies ENDOR sequence ($[\pi]_{\mathrm{inv}}$) was adjusted depending on the studied nucleus and kept constant through the experiments.

In the Mims ENDOR sequence, the resulting magnitude of the ENDOR effect is strongly dependent on the ratio between the HF coupling constant (a) and the delay between the first two MW pulses (τ): $F_{\mathrm{Mims}} \approx 1 - \cos(2\pi a\tau)$. The 2D Mims (ENDOR vs τ) method uses this blind-spot behavior to correlate the ENDOR response to the HF coupling constant a of the corresponding nuclear spin.[36,39] In this study, we have adapted this method. The 2D Mims spectrum was generated by a combination of 56 individual Mims ENDOR spectra, measured at various τ values. The data set obtained was normalized to the same baseline level. Subsequently, the baseline was subtracted with a third-order polynomial in the τ-dimension followed by fast Fourier transformation (see Figure 3).

X-band pulse EPR measurements were performed with a Bruker Elexsys E580 X-band spectrometer equipped with a SuperX-FT microwave bridge and an Oxford CF935 helium flow cryostat using a Bruker EN 4118X-MD4 dielectric ENDOR resonator and an Applied Systems Engineering 1 kW traveling wave tube (TWT) amplifier (model 117x), which allows one to use a 8 ns $\pi/2$ pulse at minimum attenuation. The X-band ENDOR spectra were recorded using the standard Bruker data acquisition system. RF pulses were generated by the Bruker "DICE" system and amplified by a 60 dB gain ENI A-500 RF amplifier. During the ^{57}Fe ENDOR measurements, the harmonics of the ^{1}H ENDOR signals (around 15 MHz) were suppressed using a low pass Trilithic RF filter H5LEC10-3-AA with a cutoff frequency of 11 MHz applied after the RF amplifier.

All Q-band measurements were performed with a Bruker Elexsys E 580 Q-band spectrometer equipped with the SuperQ-FT microwave bridge and an Oxford CF935 flow cryostat at temperatures ranging from 10 to 20 K. For these measurements, we used a slightly overcoupled cylindrical TE_{011} home-built resonator with a construction similar to that described by Sienkiewicz et al.[17,40] In this case, the minimum length of the $\pi/2$ pulse was 36 ns.

EPR Simulations. All simulations were performed using home written programs for the MatLAB environment. We used the following spin Hamiltonian for obtaining the energy levels and their wave functions for simulations of the ENDOR and HYSCORE spectra:

$$\hat{\mathbf{H}}_0 = \beta\vec{B}\cdot\mathbf{g}\cdot\hat{S} + \sum_{i=1}^{n}(-\beta_n g_n^i\vec{B}\cdot\hat{I}_i + \hat{S}\cdot\mathbf{A}\cdot\hat{I}_i + \hat{I}_i\cdot\mathbf{P}\cdot\hat{I}_i) \qquad (1)$$

where β is the Bohr magneton, β_n is the nuclear magneton, g_n^i is the g-factor of ith nucleus, and g represents the electronic g-tensor. The first and second terms in the expression correspond to the electron and nuclear Zeeman interactions with the external magnetic field; the third term describes the hyperfine interaction defined by tensor **A**, and the last term describes the quadrupole coupling defined by tensor **P**.

The quadrupole tensor **P** is traceless. The representation in its principal axes system (in frequency units) can be written as follows:

$$[P_x, P_y, P_z] = \frac{e^2qQ}{4I(2I-1)h}[-(1-\eta), -(1+\eta), 2] \qquad (2)$$

Here, we will use the two usual parameters to characterize the quadrupole coupling constants: $K = (e^2qQ)/(4I(2I-1)h)$ and $\eta = (P_x - P_y)/(P_z)$.

In all calculations, the electron Zeeman interaction was assumed to be the dominant term. All other interactions were treated as a perturbation. The orientation of the hyperfine and quadrupole tensors was defined with respect to the principal axes of the electronic g-tensor. In this study, we use the "y"-convention for rotation according to the Euler angles (α, β, γ). In this convention, the first

(35) Gemperle, C.; Aebli, G.; Schweiger, A.; Ernst, R. R. *J. Magn. Reson.* **1990**, *88*, 241–256.
(36) Schweiger, A.; Jeschke, G. *Principles of Pulse Electron Paramagnetic Resonance*; Oxford University Press: New York, 2001.
(37) Mims, W. B. *Proc. R. Soc. London, Ser. A* **1965**, *283*, 452.
(38) Davies, E. R. *Phys. Lett. A* **1974**, *A47*, 1–2.
(39) de Beer, R.; Barkhuijsen, H.; de Wild, E. L.; Merks, R. P. J. *Bull. Magn. Reson.* **1980**, *2*, 420.
(40) Sienkiewicz, A.; Smith, B. G.; Veselov, A.; Scholes, C. P. *Rev. Sci. Instrum.* **1996**, *67*, 2134–2138.

rotation is by angle α about the z axis, the second is by angle β about the new y' axis, and the third is by angle γ about the new z'' axis.[36]

The HYSCORE simulation was performed using the Matlab script described earlier.[7] The 2D Mims ENDOR experiment was simulated while operating completely in the frequency domain. The second frequency ($FT[f(\tau)]$) dimension was obtained by calculating the orientation-dependent hyperfine coupling constants and neglecting all other contributions to the spin Hamiltonian. The approach has been tested by performing similar simulations in the time domain utilizing the density matrix formalism. The results were found to be almost identical.

DFT Calculations. The geometries of complexes **A** and **C** were optimized using the Gaussian 03 program[41] utilizing one of two functionals: BP86[42−44] and B3LYP[42,45] within the spin-unrestricted DFT level. In the optimizations, Ahlrichs triple-ζ valence basis set (TZV)[46] with one set of polarization functions was used for all atoms (TZVP). No constraints were applied. Every geometry optimization was tested by IR frequency calculations. None of the presented calculations reveal any negative (imaginary) frequencies, indicating that all the structures are in minima on the potential energy surface. The resulting IR frequencies of CN and CO stretching vibrations were found to be in good agreement with available experimental data.[27−29] All geometries were obtained in the gas phase, because the introduction of an environment (at least within the Polarizable Continuum Model (PCM) methodology) does not have a substantial effect (e.g., Fe−Fe distance changes within 0.002 Å), but however considerably prolongs the calculation time.

The coordinates obtained were then used for calculations of EPR parameters using the ORCA 2.7 program[47] on the B3LYP or BP86 level (see text for details) using the resolution of the identity (RI) approximation[48,49] and using the TZV basis set with two sets of polarization functions on Fe and S and one set of polarization functions on all other atoms including hydrogens in conjunction with a corresponding auxiliary basis set.

Results

The Q-band EPR spectrum of **C** is shown in Figure 4. It is characterized by a rhombic g-matrix with principal values of 2.023, 2.004, and 1.993 (uncertainty range $\pm 5 \times 10^{-4}$), which are also consistent with X-band CW-EPR measurements (not shown). Our X-band spectrum is very similar to the one obtained by Pickett et al.[28]

^{57}Fe Hyperfine Couplings. First-hand information about the spin distribution in the di-iron cluster can be obtained via study of the ^{57}Fe hyperfine interactions. The EPR spectra of the ^{57}Fe-enriched and nonenriched complex were very similar. The line width comparison did not show any broadening for the ^{57}Fe-enriched samples, indicating that the possible ^{57}Fe HF coupling constants are smaller than the EPR line width (spectra not shown). To enhance the spectral resolution and obtain parameters of the ^{57}Fe HF couplings with high accuracy, we have applied advanced pulse EPR methods.

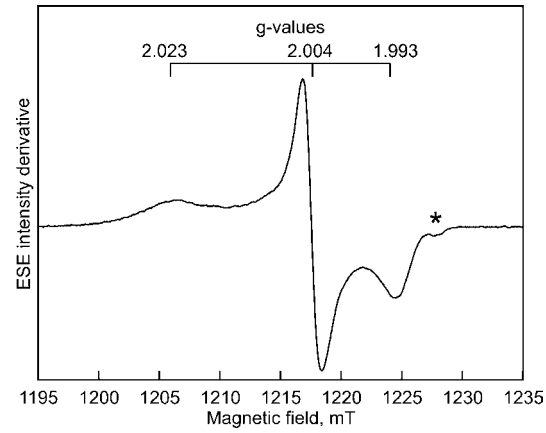

Figure 4. Pseudomodulated Q-band FID-detected EPR spectrum. Experimental conditions: temperature, 35 K; MW frequency, 34.1528 GHz; t_{mw}, 1 μs; shot repetition time, 1 ms. Spectrum is pseudomodulated with 0.5 mT modulation amplitude. The asterisk indicates an artifact, which does not correspond to the {2Fe3S} compound (possibly, a minor byproduct of the oxidation).

The best results were obtained using Mims ENDOR at X-band frequency. However, the broad ^{57}Fe signals were significantly distorted by blind spots, which is typical for this method (see Figure 3A for an example). This obscures the true shape of the signal. On the other hand, the dependence of blind spots on the delay between the first two MW pulses (τ) contains direct information about the corresponding HF coupling constants. As it was shown by de Beer et al.,[36,39] the use of the 2D Mims-ENDOR method can improve the spectral resolution and allows separation of contributing signals based on HF coupling constants (see Materials and Methods).

Figure 5 shows the resulting spectra measured at various positions of the magnetic field. As a result, two distinct signals for the ^{57}Fe nuclei have been resolved. Both signals correspond to strongly coupled ^{57}Fe nuclei with a relatively large anisotropic part of the HF tensor. The parameters resulting from the spectral simulations of the ^{57}Fe HF interactions are shown in Table 1. For simplicity of the representation, we show only the skyline projections of the simulations.

^{14}N Hyperfine and Quadrupole Couplings. A further characterization of the electronic structure of the compound was accomplished via the investigation of the spin-distribution over various ligands. The X-band HYSCORE spectra of **C** show a distinct set of ^{14}N signal in the (++) quadrant, indicating that the ^{14}N HF coupling is close to the "cancellation" regime; that is, the HF coupling matches twice the ^{14}N Larmor frequency ($2\nu_L(^{14}N) \approx A(^{14}N)$). The field dependence of the HYSCORE spectra shows that the corresponding HF coupling is rather anisotropic.

However, the complete interpretation of signals for an $I = 1$ nucleus such as ^{14}N requires the simultaneous adjustment of 11 parameters for each of the contributing nuclei because of the combination of HF and quadrupole interactions. Moreover, the complexity of the spectra prevents a unique identification of the contributing signals. To gain exclusive information about the nitrogen HF coupling constants, a compound **C** with ^{15}N labeled cyanides (compound **3***) was studied. The HYSCORE spectra of this compound show a much simpler picture due to the nuclear spin $I = 1/2$ of ^{15}N (no quadrupole coupling). Two doublet signals can be clearly distinguished and attributed to two ^{15}N nuclei (see Figure 6). As seen in the spectra, one of

(41) Frish, M. J.; et al. *Gaussian 03*, revision C.02; Gaussian, Inc.: Wallingford, CT, 2004.
(42) Becke, A. D. *J. Chem. Phys.* **1993**, *98*, 5648–5652.
(43) Perdew, J. P. *Phys. Rev. B* **1986**, *34*, 7406.
(44) Perdew, J. P. *Phys. Rev. B* **1986**, *33*, 8822.
(45) Lee, C.; Yang, W.; Parr, R. G. *Phys. Rev. B* **1988**, *37*, 785.
(46) Schäfer, A.; Huber, C.; Ahlrichs, R. *J. Chem. Phys.* **1994**, *100*, 5829–5835.
(47) Neese, F. *ORCA-an ab initio DFT and Semiempirical Electronic Structure Package, version 2.6*; University of Bonn: Germany, 2007.
(48) Eichkorn, K.; Weigend, F.; Treutler, O.; Ahlrichs, R. *Theor. Chem. Acc.* **1997**, *97*, 119–124.
(49) Eichkorn, K.; Treutler, O.; Ohm, H.; Haser, M.; Ahlrichs, R. *Chem. Phys. Lett.* **1995**, *240*, 283–289.

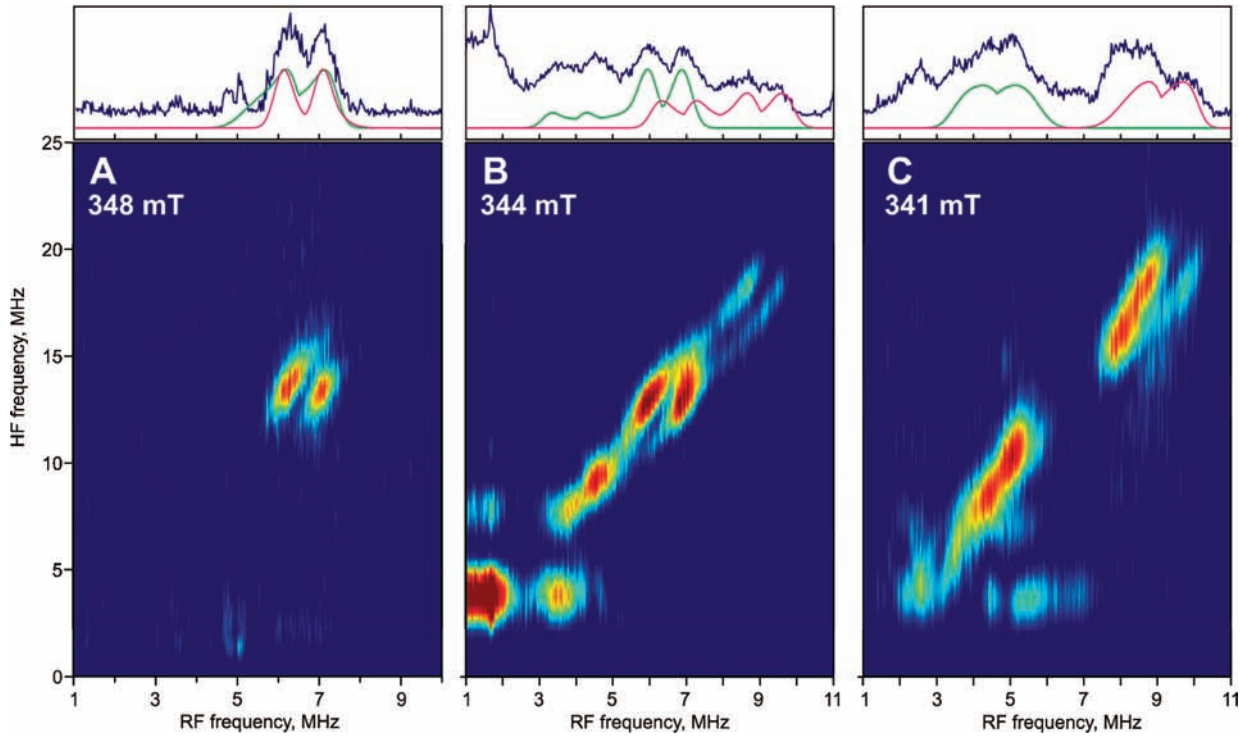

Figure 5. X-band 2D Mims ENDOR measured at various field positions. The line plots above the 2D spectra are skyline projections of the experimental spectra (blue) and simulated contributions: $A_1(^{57}Fe)$ (green) and $A_2(^{57}Fe)$ (red) HF coupling constants. Experimental conditions: MW frequency, 9.716 GHz; temperature, 35 K; $t_{\pi/2}$, 8 ns; τ_{start}, 84 ns; $\Delta\tau$, 12 ns; number of τ values, 56; t_{rf}, 20 μs; magnetic field, (A) 348 mT ($g = 1.995$); (B) 344 mT ($g = 2.018$); (C) 341 mT ($g = 2.035$, on the low field "shoulder").

Table 1. Experimentally Obtained Parameters of HF and Quadrupole Interactions of Various Nuclei

	A^a [MHz]			Euler angles [deg]					Euler angles [deg]		
	A_x	A_y	A_z	α	β	γ	K [MHz]	η	α	β	γ
$A_1(^{57}Fe)$	13.9(5)	13.9(5)	7.2(5)	0(−)	35(20)	0(30)					
$A_2(^{57}Fe)$	13.1(5)	13.1(5)	19.0(5)	0(−)	27(5)	−100(50)					
$A_3(^{15}N)$	1.3(2)	4.2(2)	1.7(2)	58(5)	−20(10)	5(10)					
$A_3'(^{14}N)$	0.9[b]	3.0[b]	1.2[b]	58(5)	−20(10)	5(10)	0.95	0	0(−)	55(10)	0(10)
$A_4(^{15}N)$	−0.15(10)	0.5(5)	0.14(10)	0(30)	0(10)	0(50)					
$A_4'(^{14}N)$	−0.10[b]	0.35[b]	0.10[b]	0(30)	0(10)	0(50)	n.r.	n.r.	n.r.	n.r.	n.r.
$A_5(CH_3)$	−2.5(3)	3.8(5)	0.5(3)	30(10)	20(10)	0(30)					
$A_5'(CD_3)$	−0.38[c]	0.58[c]	0.077[c]	30(10)	20(10)	0(30)	0.025(2)	0.8(4)	0(10)	0(10)	0(10)

[a] x,y,z coordinates are identified with respect to the following order of principal values of the g-matrix: $g_x = 1.993$, $g_y = 2.004$, $g_z = 2.023$. [b] Values for ^{14}N HFC are scaled from ^{15}N HFC, n.r. = not resolved. [c] Values for deuterium HFC are scaled from proton HFC.

the signals is due to a HF coupling close to the exact cancellation limit, while the other one is much smaller.

On the basis of the obtained ^{15}N HF couplings, the ^{14}N HYSCORE spectra were simulated adjusting only the parameters of the quadrupole coupling. The resulting parameters of the ^{14}N nuclear quadrupole and hyperfine interactions are given in Table 1.[50]

The ^{14}N HYSCORE spectra (Figure 7) were completely simulated by taking into account only one, strongly coupled, nucleus. Apparently, the signals from the weakly coupled ^{14}N nucleus are suppressed. Recently, such a suppression effect of weak signals in the presence of strong ones in ESEEM and HYSCORE spectra was described by Stoll et al.[51] The quadrupole coupling, extracted from this analysis, has a K value of 0.95, which is typical for CN^- ligands. A quadrupole coupling of similar magnitude was also found in the H-cluster.[7]

To map the spin density around the dinuclear iron center and verify the coordination of the pendant thioether, we have prepared a variant of the model in which the methyl ligand is deuterated (compound **2***). The X-band HYSCORE spectrum of this sample is presented in Figure 8B and shows intense ridges about the Larmor frequency of ^2H ($\nu_L = 2.27$ MHz at 347.6 mT). The shape of the ridges indicates substantial dipolar character of the ^2H HF coupling. The ^2H nucleus (like ^{14}N) is characterized by a nuclear spin $I = 1$, thus experiencing HF and quadrupole interactions. To better resolve the HF coupling constants, we have also performed a comparative measurement using ^1H Davies ENDOR for the labeled and nonlabeled samples (see Figure 8A).

The obtained difference spectra (A) show distinct ^1H signals that disappear upon labeling the thioether methyl group. The simulations of the difference ENDOR spectra allow us to extract exclusively the ^2H HF coupling constants corresponding to this methyl group (see Figure 8A). The parameters, obtained from this simulation, were then used to simulate ^2H HYSCORE

(50) The ^{14}N HF coupling constants were obtained from values for ^{15}N nuclei by scaling with $g_n(^{14}N)/g_n(^{15}N) = 0.7129$.
(51) Stoll, S.; Calle, C.; Mitrikas, G. *J. Magn. Reson.* **2005**, *177*, 93–101.

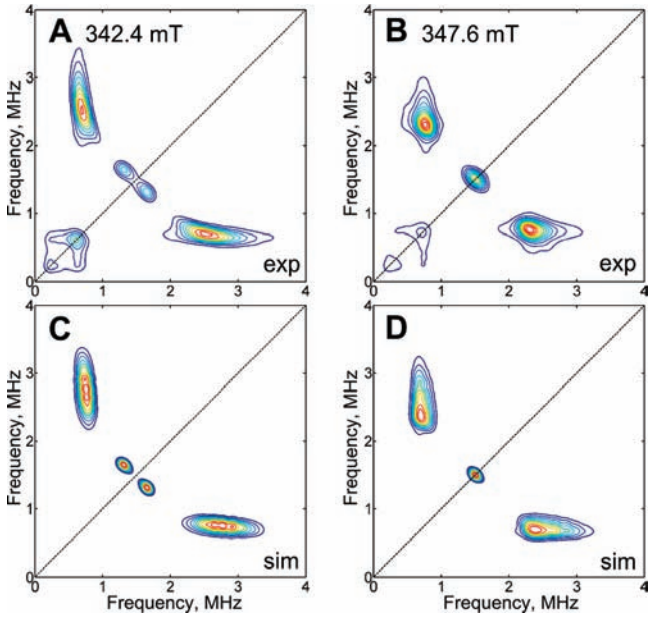

Figure 6. X-band HYSCORE spectra (only ++ quadrant is shown) of the ^{15}N-labeled model compound (**3***), measured at two field positions 342.4 mT (A) and 347.6 mT (B). The simulations of spectra A and B (C and D, respectively) were performed using the respective ^{15}N coupling constants $A_3(^{15}N)$ and $A_4(^{15}N)$ in Table 1. Experimental conditions: MW frequency, 9.7155 GHz; temperature, 20 K; shot repetition time, 7 ms; $t_{\pi/2}$, 8 ns; delay between the first and second MW pulse (τ), 280 ns; magnetic field, (A) 342.4 mT ($g = 2.027$); (B) 347.6 mT ($g = 1.997$).

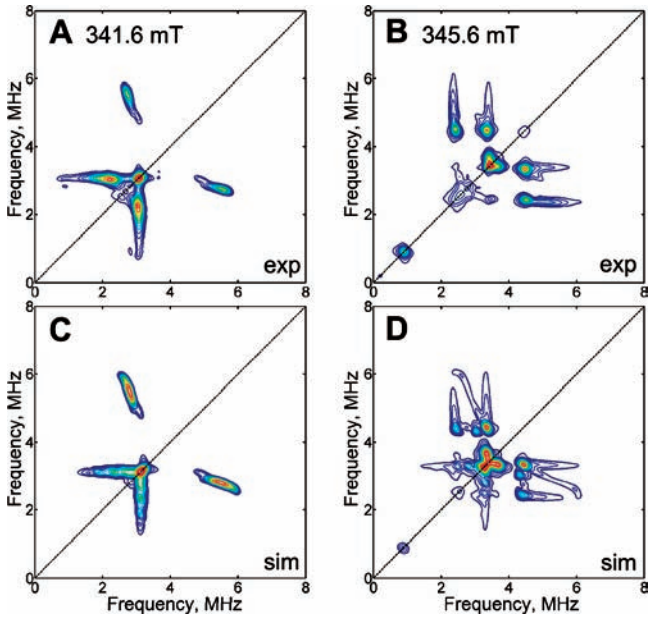

Figure 7. X-band HYSCORE spectra of the nonlabeled compound (compound **1***), measured at two field positions (A,B) and corresponding simulations using $A_3'(^{14}N)$ from Table 1 (C,D). Experimental conditions: MW frequency, 9.7138 GHz; temperature, 35 K; shot repetition time, 1 ms; $t_{\pi/2}$, 12 ns; delay between the first and second MW pulse (τ), 140 ns; magnetic field, (A) 341.6 mT ($g = 2.032$, on low field "shoulder"); (B) 345.6 mT ($g = 2.008$).

spectra obtained at six different field positions. From this analysis, the quadrupole coupling constants were extracted. Figure 8 shows one selected HYSCORE spectrum (B) with the corresponding simulation (C) of the ^{2}H signal. As a result, a single HF coupling can be extracted (see Table 1). This coupling

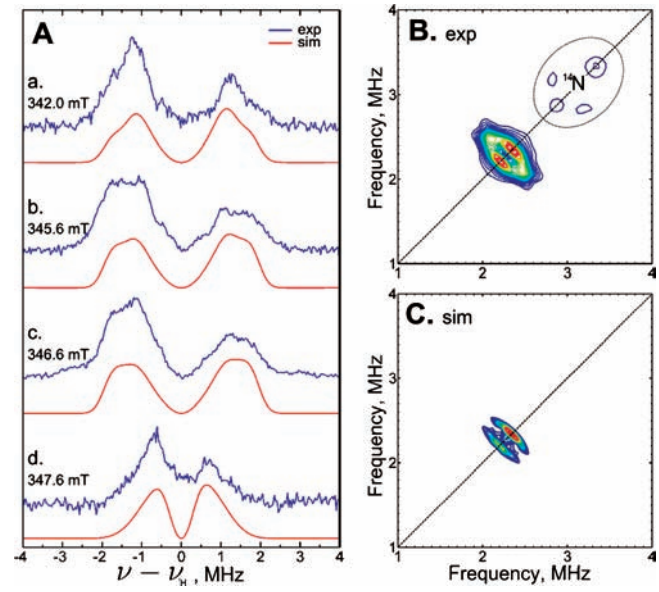

Figure 8. (A) Difference ^{1}H Davies ENDOR spectra of samples with protonated and deuterated methyl group at the thioether; (B) HYSCORE spectrum of compound **2*** ($-S-CD_3$); and (C) the corresponding simulation, accounting for a single deuterium with the parameters presented in Table 1, ($A_5(CD_3)$). Experimental conditions for spectrum A: t_{rf}, 7 μs RF; magnetic field, 342.0 mT ((a) $g = 2.029$), 345.6 mT ((b) $g = 2.008$), 346.6 ((c) $g = 2.002$), 347.6 mT ((d) $g = 1.997$); MW frequency, 9.7135 GHz; temperature, 35 K. Experimental conditions for spectrum B: MW frequency, 9.7136 GHz; temperature, 35 K; $t_{\pi/2}$, 12 ns; delay between the first and second MW pulse (τ), 140 ns; magnetic field, 347.6 mT ($g = 1.997$).

was attributed to an average coupling of three deuterium nuclei in the rotating CD_3 group, which is typical for this moiety.

DFT Calculations and Data Assignment. To assign and interpret the experimentally observed EPR signals, a set of DFT calculations on various levels of theory has been performed.

Two exchange-correlation functionals are most commonly used for DFT calculations of iron-containing inorganic molecules, BP86 and B3LYP. The former functional includes B88 as gradient-corrected exchange and P86 as correlation functional. It was found to be rather effective in representing the geometrical and vibronic structures of various compounds including metal carbonyls. It allows rather fast calculations with relatively accurate results. The hybrid B3LYP functional performs better for single point energies and EPR parameters and is currently one of the most popular ones for predicting various spectroscopic parameters of metal-containing compounds. However, a drawback of this method is the substantial increase of computation time in comparison with the BP86 level, which becomes very critical in such calculations on the complete H-cluster.

To test the necessity of using a hybrid functional such as B3LYP and to evaluate various computational methods, we have used these functionals for geometry optimization as well as for EPR parameter calculations. The recently introduced double hybrid functional B2PLYP[52] in combination with Ahlrichs TZV and QZV[53] (Fe and S: def2-QZVPP, all others TZVPP) basis set was also tested for EPR calculations. However, it showed a rather poor fit to experimental EPR data; thus, we only show it for reference in the Supporting Information. We have also found that the obtained anisotropic parts of the HF coupling in all calculations are

(52) Grimme, S. *J. Chem. Phys.* **2006**, *124*, 034108.
(53) Schafer, A.; Horn, H.; Ahlrichs, R. *J. Chem. Phys.* **1992**, *97*, 2571–2577.

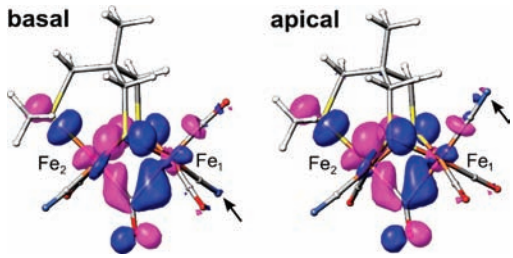

Figure 9. α-HOMO for basal (left) and apical (right) isomers of **C**, calculated on BP86 geometry-optimized structures using the B3LYP level of theory (see text for details). The position of the CN ligand at Fe_1 is indicated by arrows. The atoms color coding is the same as in Figure 1.

overestimated. We could not find any reasonable explanation for that; however, it seems to be a general problem as earlier calculations on the H-cluster also resulted in unrealistically large A_{dip} values.[54] Here, we present only the isotropic parts of the HF coupling (A_{iso}) as it is in rather good agreement with the experimental results and is essential for the discussion (the complete data sets can be found in the Supporting Information).

As shown previously based on DFT calculations by Zampella et al.[29] and later by Greco et al.,[55] the studied compound occurs in several isomers. On the basis of our calculations, the exact basal configuration of the CN ligands (*cis* or *trans*) at the two iron atoms Fe_2 and Fe_1 did not play a substantial role with respect to the single point energy (ΔE within 1 kcal/mol) as well as for the experimentally observed spectroscopic parameters (including IR frequencies). We distinguish two discrete isomers of the compound, in which the CN ligand at Fe_1 is either in a basal or in an apical position (see Figure 9). As has been already described,[29] these isomers show only small differences in the calculated single point energy ($\Delta E = 2$ kcal/mol accounting for solvent (COSMO),[29] $\Delta E = 6$ kcal/mol for gas-phase calculations); therefore, they both might occur with about equal probability. The geometries of the DFT calculated models have been verified by calculation of the corresponding IR spectra. The obtained frequencies of the CN and CO stretching vibrations are in line with those obtained previously[29,55] and available experimental data[27,28] (Figure S1 in the Supporting Information). Similar to the previously published studies, the basal isomer of **A** (Fe(I)Fe(I) variant) agrees best with the experimental data, especially in the region of the bridging CO stretching vibration. Thus, we agree with earlier results suggesting the predominant presence of the basal isomer of **A**.

To calculate the EPR parameters, mixed-valence DFT models were generated by oxidation of the reduced models and reoptimizations of the geometry. The oxidation resulted in a decrease of Fe−Fe bond distances by about 0.15 Å for all isomers, consistent with previously reported values.[29,55]

EPR parameters for all four obtained models (BP86 and B3LYP optimized geometries of both basal and apical isomers) were calculated using BP86 and B3LYP functionals resulting in eight sets of values (see Tables S1−S9 in the Supporting Information).

Independent of the used functional, both isomers show an α-HOMO (see Figure 9) that is delocalized over both iron centers as well as its ligands (including the methyl group of the thioether). The shift of the CN ligand at Fe_1 to the *trans* μ-CO position did not have a noticeable effect on the overall electronic structure.

The best agreement of the calculated A_{iso} values with the experimental data was obtained using B3LYP in combination with the TZVP (Fe and S: TZVPP) basis sets on the BP86/TZVP optimized structures. Results of the calculations are summarized in Table 2. It is worth noting that the use of the BP86 functional for the EPR calculations resulted in reasonable values as well. In fact, the BP86 predicted *g*-values are somewhat closer to the experimental values than those from the B3LYP calculations.

We can now assign the experimentally obtained magnetic couplings to certain nuclei in the model. For both considered isomers, the ^{57}Fe HF coupling constants are of similar order of magnitude, with a ratio of approximately 2:1 in favor of Fe_2. Thus, we can assign the larger experimentally obtained ^{57}Fe HF coupling to Fe_2 and the weaker one to Fe_1.

As it is shown in Table 2, the average ^{1}H coupling for the methyl group can be reproduced well especially when taking into account the relatively large error in the determination of the experimental isotropic ^{1}H HF coupling constants (see Table 1).

It turned out that DFT predicts no substantial ^{14}N HF couplings to be present for any of the two CN ligands for all models with a basal position of the CN ligand at Fe_1. On the other hand, the apical model showed a relatively large HF coupling of the CN ligand at the Fe_1, which is in excellent agreement with the experimentally observed ^{14}N coupling constants. This allows us to uniquely assign the stronger ^{14}N coupling constant to the CN ligand of the Fe_1 in the apical isomer of **C**.

Discussion

Structural Properties of the Model Compound. It has been proposed that the oxidation of the Fe(I)−Fe(I) model **B** results

Table 2. Comparison of Selected Calculated EPR Parameters Obtained Using BP86 and B3LYP Functionals for the Two Isomers of **C** (Figure 9) with Experimentally Obtained Values

	BP86		B3LYP		
	basal	apical	basal	apical	exp
		Isotropic HF Coupling Constant (A_{iso}, MHz)			
$^{57}Fe_1$	6.94	7.94	11.23	12.58	11.67
$^{57}Fe_2$	19.26	19.77	21.82	23.15	15.17
$^{14}N(CN_1)$	0.36	1.36	0.27	1.80	1.77
$^{14}N(CN_2)$	0.25	0.37	0.15	0.14	0.12
^1H (CH_3, aver)	1.00	0.96	0.43	0.38	0.60
		Principal Values of *g*-Matrix			
g_x	1.999	1.997	2.004	2.004	1.993
g_y	2.012	2.009	2.018	2.012	2.004
g_z	2.017	2.016	2.026	2.024	2.023
		Quadrupole Coupling Constants *K* (MHz) and η			
$^{14}N(CN_1)$, *K* (η)	−0.87 (0.03)	−0.89 (0.02)	−0.99 (0.03)	−0.99 (0.02)	0.95 (0.0)
$^{14}N(CN_2)$, *K* (η)	−0.88 (0.06)	−0.88 (0.06)	−0.99 (0.06)	−0.99 (0.06)	n.r

in the formation of the bridging CO ligand and coordination of the pending thioether to Fe_2 (see Scheme 1). Our data clearly confirm the binding of the thioether to Fe_2. The ^2H labeling of the methyl group of this ligand allowed us to observe the presence of spin density in that moiety. This is only possible if the thioether is connected to Fe_2; otherwise, this group would be rather far away from the spin density and no substantial HF coupling would be observable. The formation of the bridging CO has been shown by FTIR spectroscopy. Moreover, the DFT calculations, performed on the oxidized model **C**, are in good agreement with experimental data obtained earlier[27,28] and in this work. Therefore, our data support the structural changes during the oxidation of the model complex as described by Pickett et al.[27−29]

Another point, which we can address, based on the obtained data, is the isomerization of complexes **A** and **C**. As has been show earlier[29] and has been verified by our calculations (see the Supporting Information), positioning such an anionic ligand as CN^- *trans* to the μ-CO ligand shifts the corresponding CO stretching vibration frequency almost 40 cm^{-1} downward (see Figures S2 and S3 in the Supporting Information). On the basis of the comparison of the experimental and DFT calculated IR frequencies of the μ-CO ligand, Zampella et al. have concluded that the isomer with basal configuration of CN^- ligands is predominant in compound **A**.[29] Our IR examination of compound **A** in butyronitrile shows FTIR spectra similar to those reported by the group of Pickett.[27,28] Close inspection of the frequency region down to 1710 cm^{-1} did not reveal any additional bands attributable to the μ-CO ligand of the apical isomer of **A** (data not shown). Thus, we agree with Zampella et al. that compound **A** is predominantly in a form where both CN ligands are *trans* to μ-SR (basal isomer). On the other hand, our pulse EPR studies on compound **C** reveal a well-defined signal from ^{14}N that (based on DFT calculations) is only consistent with the isomer where CN^- is *trans* to the μ-CO ligand (apical isomer), coinciding with the d_{z2}-like HOMO on Fe_1. On the basis of the strength of the ^{14}N signals in the ENDOR and ESEEM spectra assigned to the apical isomer, we suggest that this isomer is the dominant one in the sample.

We have investigated the complex in two solvents: butyronitrile and acetonitrile. The dielectric constants of these solvents differ considerably ($\varepsilon = 20.7$ versus $\varepsilon = 37.5$ at room temperature). However, both samples showed remarkably similar EPR and almost identical ^{14}N ESEEM/HYSCORE spectra (not shown). This indicates that the polarity of the solvent (at least in these cases) does not affect the arrangement of ligands or the ratio between different isomers.

We had no possibility to test compound **C** in our preparations using IR spectroscopy. However, earlier IR studies have shown that the basal isomer is indeed present in the sample.[27] Unfortunately, the lower frequency region has not been shown in that publication. Therefore, we cannot verify whether the apical isomer was present as well. Nevertheless, it is apparent that at least under our experimental conditions the equilibrium between the two isomers shifts toward the apical isomer upon oxidation. In fact, such isomerization effects are not uncommon in [FeFe] hydrogenase model chemistry and have been described by, for example, Justice et al.[56] on models for the H_{ox}−CO state containing bidentate phosphine ligands.

Electronic Structure. On the basis of previous studies, it was shown that due to the CO/CN ligands, the iron atoms are anticipated to be in a low spin state.[1,21] In that case, Fe(I) and Fe(III) would have a doublet ground state ($S = 1/2$), while for Fe(II) it is a singlet ground state ($S = 0$). It was also shown that complex **C** is characterized by an $S = 1/2$ EPR spectrum, which is indicative of a mixed-valence Fe(I)−Fe(II) state. In the spin-localized case, one expects to observe a single strongly coupled ^{57}Fe nucleus for Fe(I) and a much weaker (presumably dipolar) ^{57}Fe interaction for the second iron Fe(II). However, our observation shows two rather strong HF couplings of ^{57}Fe, indicating a delocalization of the spin-density over both iron centers. This is supported by the theoretical calculations. With respect to the ^{57}Fe HF couplings, the theory predicts a somewhat more localized case than is observed in the experiment, showing a HF coupling at Fe_2, which is about twice as large as that at Fe_1, while in the experiment this ratio is smaller (about 5:4). Nevertheless, the composition of the frontier orbitals contains substantial contributions from both iron centers (see the Supporting Information). Moreover, Mulliken and Löwdin population analyses (as implemented in Orca 2.7) consistently show very similar atomic charges on both iron atoms. Therefore, we incline to describe the valence state of the model as delocalized, that is, $Fe_2(I+\delta)-Fe_1(II-\delta)$, where δ is close to 0.5. The formal oxidation states we can only assign on the basis of the somewhat larger spin density population on Fe_2 than Fe_1. We believe that further studies using ^{57}Fe Mössbauer spectroscopy can clarify this point.

In addition, we have found a large contribution of sulfur centered orbitals in the HOMO in both isomers irrespective of the level of theory used. Therefore, it is anticipated that modifications of these ligands might have a substantial effect on the properties of the model compound. This coincides with the fact that changing the moiety of the bridgehead might considerably change the catalytic properties of the model cluster, in particular its redox potentials.[21,24]

Comparison with the H-Cluster. As this model compound is structurally rather similar to the binuclear part of the H-cluster in the H_{ox}−CO state, it is interesting to compare their electronic structures.

In the "native" cluster, CO inhibition of the H_{ox} state has been shown to shift the spin density in the binuclear subcluster toward the proximal iron, resulting in large changes in the ^{57}Fe HF couplings and an almost 4-fold increase in the $[4Fe4S]_H-[2Fe]_H$ exchange coupling.[16,17,57,58] Therefore, in contrast to model complex **C**, which shows a more or less symmetric spin distribution (5:4) over the two iron centers, the binuclear subcluster in the H_{ox}−CO state exhibits an asymmetric spin distribution (approximately 5:1), centered at the proximal iron.

It is interesting to note that earlier DFT calculations of the electronic structure of the H-cluster in the H_{ox}−CO state[54] show an almost symmetric distribution of the spin-density over the two iron centers. In addition, it was shown that DFT (at least using the broken symmetry (BS) approach) predicts only a marginal influence of the $[4Fe4S]_H$ subcluster on the electronic structure of the binuclear subcluster. The obtained distribution of spin densities in $[2Fe]_H$ of the H_{ox}−CO state model is in fact very similar to the

(54) Fiedler, A. T.; Brunold, T. C. *Inorg. Chem.* **2005**, *44*, 9322–9334.
(55) Greco, C.; Bruschi, M.; Fantucci, P.; De Gioia, L. *J. Organomet. Chem.* **2009**, *694*, 2846–2853.
(56) Justice, A. K.; Nilges, M. J.; Rauchfuss, T. B.; Wilson, S. R.; De Gioia, L.; Zampella, G. *J. Am. Chem. Soc.* **2008**, *130*, 5293–5301.
(57) Pereira, A. S.; Tavares, P.; Moura, I.; Moura, J. J. G.; Huynh, B. *J. Am. Chem. Soc.* **2001**, *123*, 2771–2782.
(58) Silakov, A.; Wenk, B.; Reijerse, E.; Albracht, S. P. J.; Lubitz, W. *J. Biol. Inorg. Chem.* **2009**, *14*, 301–313.

one obtained in this work for the {2Fe3S} model (see Figure S4 in the Supporting Information). On one hand, it shows that from a DFT point of view the $[2Fe]_H$ and {2Fe3S} constructs are very similar. On the other hand, experimentally the cases are clearly different. Not only the magnitude of the ^{57}Fe HF couplings is different, but also the ratio of the couplings from the two iron sites, which is indicative of differences in the unpaired spin distributions in $[2Fe]_H$ and the {2Fe3S} model. Thus, the ^{57}Fe HF coupling values of the H-cluster and the {2Fe3S} model cannot be related to each other simply by introducing a uniform scaling factor.[59] Apparently, the presence of the $[4Fe4S]_H$ cluster does not only result in a trivial exchange-induced level-mixing but in a rather complex modification of the MO's in the $[2Fe]_H$ cluster leading to a change in the unpaired spin distribution, which cannot be correctly predicted by DFT (including BS) methods. Certainly, some deviation of the spin distribution between the native and the model systems might also result from the amino acid surrounding of the H-cluster; however, no substantial effect could be observed in our DFT calculations so far (work in progress).

Although the protein surrounding might have only a minor influence on the electronic structure, it can still influence the ability of the H-cluster to isomerize. On the basis of the studies of various model compounds, it was proposed that a rotational isomerization of ligands at the distal iron of the $[2Fe]_H$ might allow switching between bridging and terminal CO ligation.[21] It was also proposed that this, in turn, would allow formation of a bridging hydride during the heterolytic splitting of molecular hydrogen.[60] Similarly, apical and basal isomers alternating with the oxidation state of the irons can be distinguished in the {2Fe3S} model of the H_{ox}−CO state in our study. On the basis of the obtained data, we can conclude that the model and its prototype are structurally very similar. However, in the H_{ox}−CO state of the H-cluster, no strongly coupled ^{14}N (CN) signal could be resolved that would indicate the presence of an apical isomer.[7] Instead, a strong ^{13}C HF coupling of the CO_{ext} was observed.[58] This indicates the presence of a single isomer in which a CO ligand is at the *trans* position to μ-CO (apical) and CN ligands are in basal positions. Moreover, EPR and FTIR spectra of the H_{ox} state would change considerably upon rotational isomerization of its ligands due to a shift of the bridging CO ligand to the terminal position at Fe_d. However, all the available experimental data show no sign of alteration from the conventional structural model. As was proposed earlier on the basis of X-ray crystallographic data[2,3,8,9,13] and supported by our recent work,[7] there is a strong H-bond between the distal CN ligand and the side chain of a Lys residue. Thus, it is likely that the H-bonding is stabilizing the CN in that basal position and prevents the isomerization. We believe that this has a dramatic effect on the catalytic mechanism; for example, it might prevent the formation of a bridging hydride during heterolytic splitting. Our recent ^{14}N HYSCORE study has verified the presence of nitrogen as the central atom in the dithiol bridge that can act as a base for heterolytic splitting.[7] In addition, an IR spectroelectrochemical study of the HydA1 [FeFe] hydrogenase from *C. reinhardtii* has shown that the H_{ox}/H_{red} redox transition does not necessarily result in a shift of the bridging CO to the terminal position.[6] All together, the data point to a mechanism in which the heterolytic splitting occurs exclusively at the open coordination site of the distal iron.

(59) The magnitude of the ^{57}Fe HF couplings observed for the H-cluster are decreased due to [4Fe4S]−[2Fe] exchange interaction. Therefore, in the comparison with the model system, one should take this effect into account by introducing a uniform scaling factor.

(60) Bruschi, M.; Zampella, G.; Fantucci, P.; De Gioia, L. *Coord. Chem. Rev.* **2005**, *249*, 1620–1640.

Summary and Conclusions

We have performed an extensive EPR characterization of a {2Fe3S} model compound resembling the binuclear subcluster of the active site of the [FeFe] hydrogenase in its CO-inhibited state. Additionally, we have performed a set of theoretical calculations to rationalize the obtained data. It was found that DFT calculations of this dinuclear model produce results that are in good agreement with the experimental data. On the basis of these findings and their comparison with earlier studies, we can conclude the following:

(i) The DFT calculations show a particularly good agreement with respect to the measured isotropic HF interactions of the iron core and the ligand nuclei; thus, the electronic spin density distribution is represented well on the used level of theory.

(ii) Two ligand isomers of the model complex can be distinguished, based on the position (basal or apical) of the CN^- ligand of the iron, distal to the thioether. While in the reduced state the basal isomer is dominant, upon oxidation to the EPR active state, the "distal" CN moves into the apical position. However, comparison of the EPR data from the model and the H-cluster in the H_{ox}−CO state suggests that the CN^- ligand isomerization does not occur in the active site of the [FeFe] hydrogenase.

(iii) In the studied model complex, the electron spin density is delocalized over both irons. Theory shows a delocalization of frontier molecular orbitals. This leads to the conclusion that the oxidation state of the irons must be delocalized as well leading to a $Fe_2(I+\delta)-Fe_1(II-\delta)$ configuration where δ is close to 0.5.

(iv) On the basis of the comparison of the obtained results with those of the native H-cluster we can conclude that the formally diamagnetic $[4Fe4S]_H$ cluster has a substantial influence on the electronic structure of the paramagnetic $[2Fe]_H$ that cannot be correctly represented by the BS DFT levels of theory.

Acknowledgment. We would like to acknowledge Prof. C. Pickett (University of East Anglia, United Kingdom) for helpful discussions and advice on the synthesis of the compounds. We would also like to thank G. Klihm and F. Reikowski (both MPI, Mülheim an der Ruhr, Germany) for their technical assistance in the EPR measurements. This project has been supported by the Max Planck Society and the EU/Energy Network project SOLAR-H2 (FP7 contract 212508).

Supporting Information Available: Figures representing relations between states of the H-cluster, complete X-band HYSCORE spectrum of the **2*** compound, and comparison of MO's for apical and basal isomers of the {2Fe3S} subcluster; a full set of calculated values of HF couplings for various nuclei; the comparison of Fe−ligand and Fe−Fe distances for the calculated geometries of the compound; tables showing population analyses; DFT calculated IR spectra; tables with *g*-matrix direction cosines; Cartesian coordinates of the calculated geometries, and complete ref 41. This material is available free of charge via the Internet at http://pubs.acs.org.

JA107793E